Coastal Dynamics 2017
Paper No. 072

WAVE RUNUP OVER THE STEEP ROCKY CLIFFS OF BANNEG ISLAND, FRANCE

Guillaume Dodet[1], Fabien Leckler[2], Fabrice Ardhuin[3], Serge Suanez[1] and Jean-François Filipot[4]

Abstract

The wave runup is known to depend on the offshore wave conditions and the beach slope. While most field studies on wave runup have focused on low-to-mild sloping sandy beaches, runup measurements on steep and irregular rocky beach profiles are still very sparse. Hence, little is known on the physical processes affecting the wave runup in such environments, and the range of applicability of empirical runup formula requires further investigation. This study focuses on the steep ($0.1 < \tan\beta < 0.4$) rocky cliffs of Banneg Island, a small island of the Iroise Sea occasionally flooded during extreme water level events. A statistical parameter for extreme runup is derived from the measurements of pressure sensors deployed in the intertidal zone. Deep water wave parameters and high-resolution topographic data are analyzed concurrently with runup time-series in order to assess the dependence of the runup on hydrodynamic conditions and foreshore slopes. The wave runup is shown to be strongly related to the surf-similarity parameter times the offshore significant wave height. Given the large topographic variability of the beach profile, the method used to compute the beach slope is shown to strongly affects the results.

Key words: wave runup, rocky coasts, steep slopes, pressure sensor measurements, Banneg Island

1. Introduction

The foreshore is alternatively covered by water and exposed to the air as the water rushes up and washes back. The runup represents the vertical excursion of the water's edge across the foreshore, and its wave component (excluding tides and storm surges) is commonly decomposed into a steady component, the wave setup, and a fluctuation about this setup, the swash. When storm waves are combined with high water levels, the wave runup can reach unexpected elevations and becomes a hazard for coastal infrastructure and populations, through dike overtopping, dune breaching or accelerated coastline erosion (Sallenger, 2012; Ruggiero *et al.*, 2013; Suanez *et al*., 2015). In a pioneering effort to provide guidance for the design of coastal defense structures, Hunt (1959) analyzed laboratory data and derived an empirical relationship between the maximum runup R, the slope of the structure β, and the offshore significant wave height H_0 and wave length L_0,

$$\frac{R}{H_0} = K \frac{\tan\beta}{\sqrt{H_0/L_0}} \tag{1}$$

Later, Battjes (1974) synthesized the results of numerous studies on surf zone processes, such as the ones of Iribarren and Nogales (1949), Hunt (1959) and Bowen *et al*. (1968), and highlighted the central importance of the righ-hand side of Eq.1 for governing wave breaking, setup and runup processes. This non-dimensional surf-similarity parameter ξ_0, commonly called the Iribarren number, is

$$\xi_0 = \frac{\tan\beta}{\sqrt{H_0/L_0}} \tag{2}$$

Most of the studies dedicated to wave runup that followed the work of Hunt (1959) have been based on field data collected on sandy beaches, with foreshore slopes ranging from 0.02 to 0.2 (Huntley *et al*., 1977; Guza and Thornton, 1982; Holman and Guza, 1984; Holland *et al*., 1995; Raubenheimer and Guza, 1996; Ruessink *et al*., 1998; Senechal *et al*., 2011; Vousdoukas *et al*., 2012). Hence, very few runup field measurements exist for steeper slopes ($\tan \beta > 0.2$) that are encountered on gravel beaches and rocky cliffs. Poate *et al*. (2016) analyzed video-based runup measurements on gravel beaches, with slopes up to 0.4. They obtained strong correlation between the wave runup and the offshore significant wave height, the mean wave period, the beach slope and the grain size, in decreasing order of importance. They also found that the widely-used runup equation of Stockdon *et al.* (2006) strongly underestimated the runup when it was applied to their field conditions. Meer and Stam (1992) investigated the influence of rock slopes on the wave runup over coastal structures, for slopes ranging between 0.05 and 0.25. They compared laboratory data of runup on smooth and rocky structures and showed that the runup on rock slopes could be reduced by up to 50% compared to the results obtained on smooth slopes, for Iribarren numbers comprised between 0.5 and 2. These results raised the need to acquire runup observations on natural rocky environment, for a wide range of conditions, in order to test the validity of existing runup equation in these environments.

The present study is based on field data recorded during winter 2014/15 over the steep rocky cliffs of Banneg Island. This small uninhabited island located in the Iroise Sea is often subjected to very stormy conditions, and its central part has been occasionally overwashed during extreme wave runup events (Suanez *et al*., 2009; Fichaut and Suanez, 2011; Autret *et al*., 2016). In section 2, we describe the environmental context of the island and the field survey. In section 3, we present the methods that we used to compute the offshore wave parameters, the foreshore slopes, and the extreme runup statistics inferred from the pressure sensor records. In section 4, we use high resolution topographic data and continuous measurements of offshore wave parameters to compare the estimated runup time-series with incident wave conditions and foreshore slopes, computed on various segments of the beach profile. Finally, we discuss the relation obtained between the normalized wave runup and the Iribarren number over the rocky cliffs of Banneg Island to the light of previous studies (Section 5).

2. Banneg Island

2.1. Geomorphological context and hydrodynamic conditions

Banneg Island is located in the Iroise Sea, off the western tip of Brittany peninsula (Fig.1). It lies in the north-western edge of the Molène archipelago, which is separated from Ouessant Island by the 60-m deep Fromveur Channel. This small island constitutes a granite batholith, oriented north-south, 0.8 km long and 0.15 to 0.35 km wide. The western coast is cut into steep cliffs ($\tan \beta > 0.5$) made up of a series of high headlands (16 m to 20 m above mean sea level, AMSL), and lower (12 m to 13 m AMSL) and less steep cliffs ($0.15 < \tan \beta < 0.4$) in embayments. These cliffs present an orthogonal tabular structure resulting from the horizontal bedding and nearly vertical joint system affecting the granite bedrock. Large boulder accumulation, quarried from the cliff top, lay over the bedrock and contribute to the rugged morphology of the western part of the island. The Iroise Sea is characterized by a semidiurnal macro-tidal regime with tidal ranges from 2 m to 8 m in neap and spring tide conditions, respectively (SHOM, 2014). The irregular coastline and the presence of numerous islands induce very strong tidal currents in this area. Near Banneg, the maximum tidal range is 7.9 m and tidal currents in the Fromveur Channel can exceed 4 m.s -1 during spring tides (SHOM, 2016). The area around Ouessant Island is likely the part of the French coastline most exposed to waves. The wave buoy Les Pierres Noires (5.0°W ; 48.2°N ; 60-m depth, WMO number 62069) recorded significant wave height (H_s) larger than 12 m (e.g. during Ruzica storm on February, 2015) and winter-averaged H_s comprised between 2.1 m and 3.7 m, from 2008 to 2016. On Banneg's shores, waves are attenuated by the sheltering effect of Ouessant Island. The results of a 14-year (1993-2013) high-resolution regional wave hindcast (Boudière *et al*., 2013; Roland and Ardhuin, 2014) indicate that the winter-averaged H_s, peak period (T_p) and mean wave direction (θ_m), 1 km west of Banneg Island, are 1.8 m, 11.8 s and 242.9°, respectively. During this period, the simulated H_s never exceeded 7 m. Ardhuin et al. (2012) also showed that the tidal currents in the Fromveur Channel have a strong influence on the propagation of incident waves due to current-induced wave refraction and dissipation, and the blocking of

high-frequency waves in opposite currents.

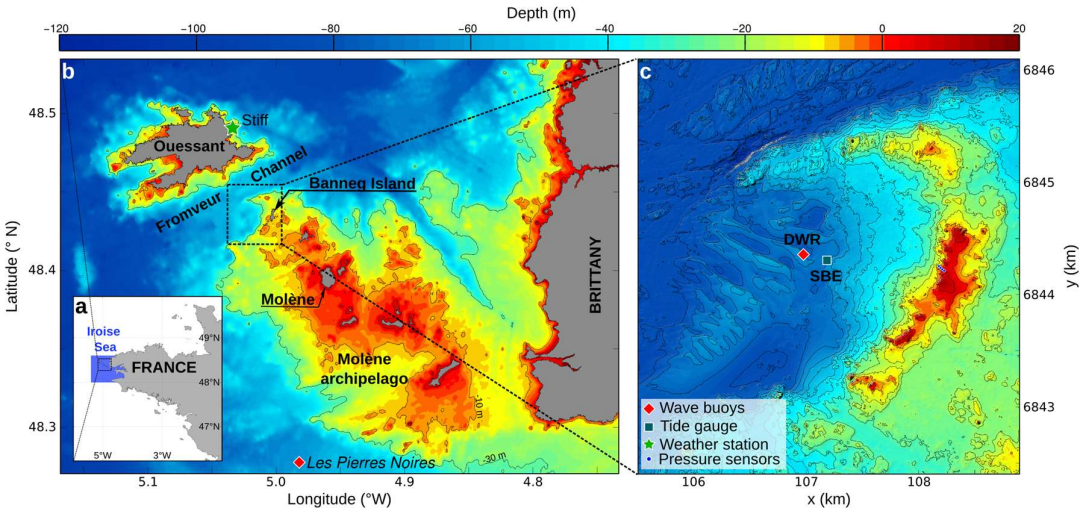

Figure 1. (a) Location of the Iroise Sea (blue area) and the Molène archipelago (black rectangle). (b) Location of Banneg Island and bathymetry of the Molène archipelago. (c) Topography and bathymetry of Banneg Island (isolines are given every 5 meters).

For more than two decades, Banneg Island has been investigated by geomorphologists, who put in evidence the strong morphogenic impacts of storm waves on the island. Indeed, more than 1000 m^3 of cliff-top storm deposits (CTSD), weighing up to 30 tons, were quarried from the cliff-top and accumulated at the rear of the embayments, with the furthest accumulation lying 100 m inland (Fichaut and Hallégouët, 1989; Suanez *et al*., 2009; Fichaut and Suanez, 2011). Autret *et al*. (2016) carried out a detailed analysis of 149 CTSD trajectories from pre- and post-storm drone-based surveys. They related these trajectories to synchronous hydrodynamic measurements in order to detect the morphogenic overwashing events that occurred during winter 2013/14. They also derived runup estimates from a calibrated empirical formula and found maximum values higher than 15 m in some parts of the island.

2.2. Field survey

During winter 2014/15, a 4-month field survey was carried out at Banneg Island in order to characterize offshore and nearshore hydrodynamic conditions. A directionnal waverider (Datawell DWR-MkIII, hereafter referred to as DWR) and a bottom-mounted pressure sensor (Seabird Electronics SBE26+, hereafter referred to as SBE) were deployed 1 km offshore west of Banneg Island, in approximately 50-m water depth (Fig. 1c). They measured wave parameters and tidal elevations from November 18, 2014 to March 18, 2015. Four pressure transducers (Ocean Sensor System, OSSI-010-003C) were installed along a cross-shore profile within an embayment of the western part of the island, (Fig. 1c). Each sensor was held in a stainless steel support itself attached to the bedrock with sealed threaded rods. The sensor's height above the bed was fixed by the dimension of the support and was approximately 12 cm. Hereafter, the pressure sensors will be named P_1, P_2, P_3 and P_4, from the bottom to the top of the cliff, respectively (Fig.2). The pressure sensors recorded the pressure variations of the water-plus-air-column (when immersed) and of the air-column (when emersed) continuously at 5 Hz, from January 23, 2014 to April 20, 2015.

3. Data Processing

3.1. *Offshore parameters*

Offshore water levels were estimated from the SBE tide gauge that provided 2-min averages of water elevation every 20 min. After adjusting the raw pressure for the atmospheric pressure (measured at the Stiff weather station, on Ouessant Island, see Fig.1b) and converting the water pressure into water elevation assuming hydrostaticity, the 4-month mean was subtracted from the corrected time-series in order to reference the water elevation with respect to MSL. For consistency with bathymetric and topographic information, all hydrodynamic observations were referred to the IGN69 topographic French datum. Offshore bulk wave parameters (H_s, θ_m, T_p, $T_{m0,1}$, $T_{m0,2}$, $T_{m0,-1}$ and $T_{m0,-2}$) were estimated from the directional spectra measured by the DWR.

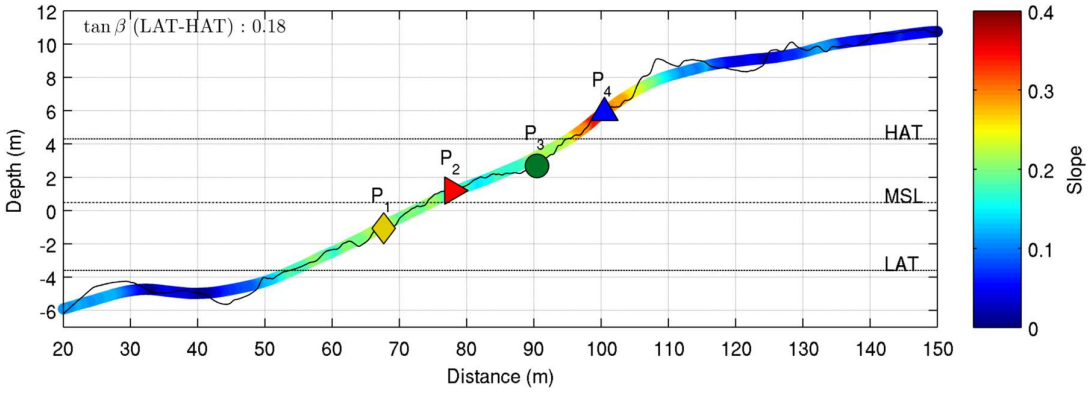

Figure 2. Bathymetry/topography of the cross-shore profile. The black line corresponds to the profile used to compute the slopes. The thick colored line corresponds to a smooth profile computed with a 20-m wide moving average, and shows the large scale topographic gradient (not used hereafter). The location of the four sensors are indicated with colored symbols.

3.2. *Nearshore parameters*

Nearshore wave parameters were computed from the pressure sensor P_1 located at the bottom of the profile, which acquired hydrodynamic data in a maximum of 5.3 m water depths, during spring high tides. The spectral analysis was carried out on a 20-min window sliding along the whole time-series. Pressure elevation spectra were computed on 50%-overlapped segments of 1024 samples, detrended and tapered with a Hanning window to suppress tidal motions and reduce spectral leakage. The resulting spectra had a spectral resolution of 0.005 Hz, a bandwidth of 2.49 Hz (0.01 Hz - 2.5 Hz) and 12 degrees of freedom. The pressure Fourrier coefficients were then converted into sea surface elevation spectra based on linear wave theory. Finally, the significant wave height was computed using the cut-off frequency f_{max} = 0.35 Hz, to remove high frequency noise. In the remaining of the paper H_s will refer to the nearshore significant wave height measured by the bottom pressure sensors and H_0 will refer to the offshore significant wave height measured by the waverider.

3.3. Estimation of η_2

The pressure sensor records were analyzed to infer an extreme value statistical parameter for wave runup. Once the atmospheric pressure was subtracted from the raw signal, swash bores appeared as individual pikes separated by longer and nearly-flat pressure records, fluctuating about zero (Fig.3). Our method consisted in detecting the 20-min time periods, during which the sensor was immersed 2% of the time only. Then, the extreme wave runup parameter was computed as the difference between the elevation of the sensor and the still water level averaged over this time window. This vertical distance corresponds to the 2% exceedence level of shoreline elevation, η_2, as defined by Holman (1986). These authors named this parameter η_2, to distinguish it from R_2, which is computed from the distribution of individual maxima of shoreline elevation. The variable name η_2 is also be adopted in this study, and the term extreme wave runup refers to it, since no other extreme value statistics for the runup is analyzed. Because of the inherent accuracy and resolution of the instruments, and the uncertainty on the local atmospheric pressure (the

weather station used to correct the data was located 5 km away), the pressure measured by the sensors when they were dry was not strictly equal to zero, but noisy and slightly biased. η_2 estimates were thus obtained when the 20-min time periods, during which the 1.5% and 2.5% exceedence levels were respectively higher and lower than a threshold value ε. This threshold value was obtained by computing the means ($<p_0>$) and the standard deviation (σ) of a large amount of 20-min bursts, recorded when the sensors were dry, and using the maximum values as follows :

$$\varepsilon = <p_0>_{max} + 2\sigma_{max} \quad (3)$$

Assuming a gaussian distribution of the noise, using $2\sigma_{max}$ ensured our threshold to be higher than 95.4% of the dry samples. Fig.3 illustrates the methodology applied to a 20-min sample.

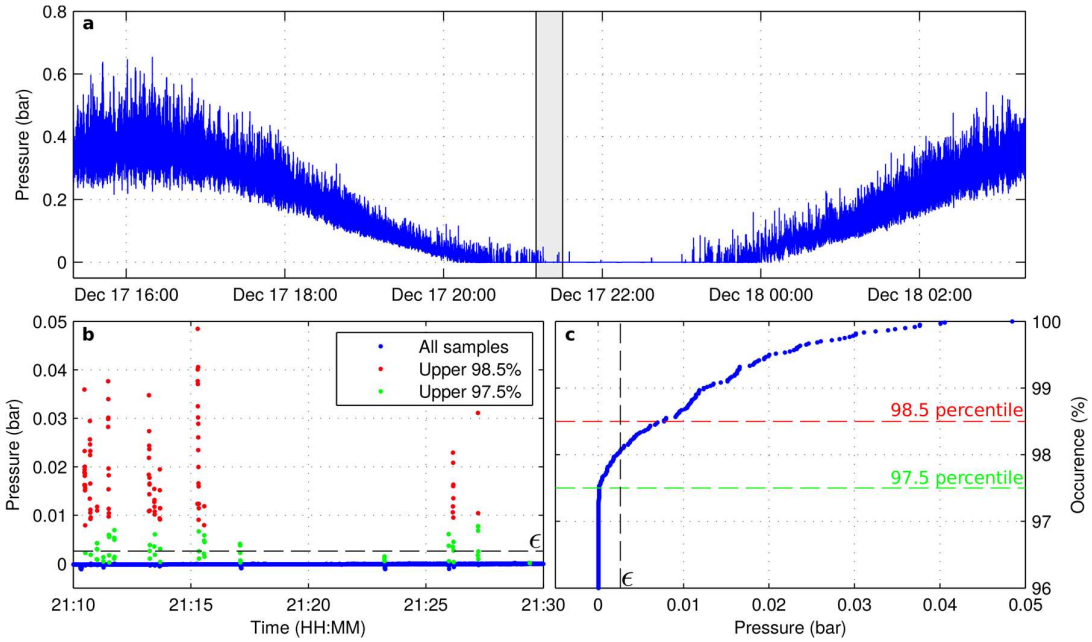

Figure 3. (a) 12-hr time-series of pressure measurements, during which, one η_2 value was computed, (b) 20-min burst of pressure data (shown in grey in panel a) during which the 98.5 (resp. 97.5) percentile was higher (resp. lower) than (dashed black line), (c) cumulative distribution of the 20-min pressure data showing the intersection between the data and occurring within the 98.5 and 97.5 percentiles. η_2 is then computed as the difference between the sensor elevation and the still water level measured during this period.

3.4. Computation of the foreshore slopes

Many studies showed that the wave runup is dependent on the foreshore slope, whether from laboratory experiments (Hunt, 1959; Meer and Stam, 1992; Blenkinsopp *et al*., 2016), or field data (Holman, 1986; Stockdon *et al*., 2006; Suanez *et al*., 2015; Poate *et al*., 2016). For this latter case, several methods were proposed to compute the slopes on irregular profiles and/or macrotidal environments. Holman (1986) computed the foreshore slope as the average slope over a 5-m wide region surrounding the mean sea level. Stockdon *et al*. (2006) defined the foreshore slope as the average slope over a region ±2σ around <η>, with σ the standard deviation of the continuous shoreline elevation, and <η> the average shoreline elevation (i.e. the still water level plus the wave setup). Other authors used the offshore significant wave height as a proxy for the swash zone extent and computed the foreshore slope on a time-varying section varying with the tide and wave conditions. Yet no consensus arose from the literature about which fraction of H_0 should be used in this respect. For instance, Suanez *et al*. (2015) used the still water level (SWL) ± 0.25 H_0 for the upper and lower bounds of the profile section, while Poate *et al*. (2016) used SWL + H_0 for the upper bound and SWL - 2 H_0 for the lower bound. These field studies were mostly conducted on sandy coasts,

characterized by relatively smooth topographic gradients. On rocky coasts exposed to waves, such as the western coast of Banneg Island, sharp topographic gradients may occur at both small and large scales, due to the presence of boulders, headlands and embayments. As a consequence, the slopes estimates may strongly differ from one method to another, and so may the associated results. Several methods to compute the beach profiles were thus tested in this study. The bathymetric and topographic data was retrieved from a high-resolution digital elevation model, continuous at the land-sea interface, acquired with airborne lidar and vessel-mounted multi-beam sounders (Litto3D, Louvart and Grateau, 2005). A 200-m long profile starting from the top of the cliff and intersecting the highest and lowest sensors was interpolated at 0.5 m resolution (Fig.2). Then, the slopes were computed with a linear regression fitted through the beach profiles over a region dependent on the selected method. Five methods were defined and are listed below in increasing order of complexity :

— for the first method (M_1), we considered a segment vertically bounded between the lowest astronomical tide (LAT) and the highest astronomical tide (HAT) levels. This method provided stationary slopes, identical for the two sensors of a same profile, and was used as a baseline to compare with the four following method;

— for the second method (M_2), we considered a 50-m wide segment right-bounded by the profile intersection with the instrument's position, which always corresponds to SWL + η_2. This method provided stationary slopes, dependent on the sensor's location only;

— for the third method (M_3), we considered a 50-m wide segment horizontally centered on the intersection between SWL and the profile. This method provided time-varying slopes, dependent on the tide, but independent of the wave conditions, similar (except for the chosen width) to the one of Holman (1986) ;

— for the fourth method (M_4), we considered a segment vertically bounded by SWL + H_0, for the upper bound, and SWL - $2H_0$ for the lower bound. This method provided wave- and tide-dependent slopes, similar to the one used by Poate et al. (2016) ;

— for the fifth method (M_5), we considered a segment vertically bounded by SWL ± η_2. This method provided runup- and tide-dependent slopes, computed over a segment that approximated the swash zone extent, as in Stockdon et al. (2006).

In methods M_2 and M_3, several segment widths were tested iteratively, and our selection (50 m) was based on the results described in Section 4.3.2.

4. Results

4.1. Offshore wave conditions and water levels

Offshore water levels and wave conditions were measured simultaneously by the DWR and SBE instruments (Fig.4). During the four-month period of measurements, the tidal range was comprised between 2.4 m and 7.6 m, and the mean H_0 was 1.6 m. Only two storms generated waves with H_0 exceeding 4 m, with a maximum of 5.4 m on January 14. Based on a long-term wave hindcast, Boudière *et al*. (2013), found a winter mean H_0 of 1.8 m and a maximum H_0 of 7 m at the same location, for the period 1993-2014. This winter was thus relatively calm, especially in comparison with the preceding exceptional winter 2013/14 (Masselink *et al*., 2016), which was characterized by an almost uninterrupted succession of storms (Blaise *et al*., 2015). The wave period $T_{m0,-2}$ was 9.5 s on average and reached up to 16.2 s. The mean wave direction (θ_m) was 256° on average, and was strongly modulated by the tide (σ = 43°) with amplitudes of the modulations exceeding sometimes 40°. Offshore water levels and wave direction were in phase quadrature, indicating that current-induced refraction occurred with maximum flood and ebb currents. The significant wave height also appeared to be significantly modulated by the tidal currents, with H_0 usually larger during flood than during ebb, likely as a result of enhanced wave dissipation over negative current gradients (Phillips, 1984).

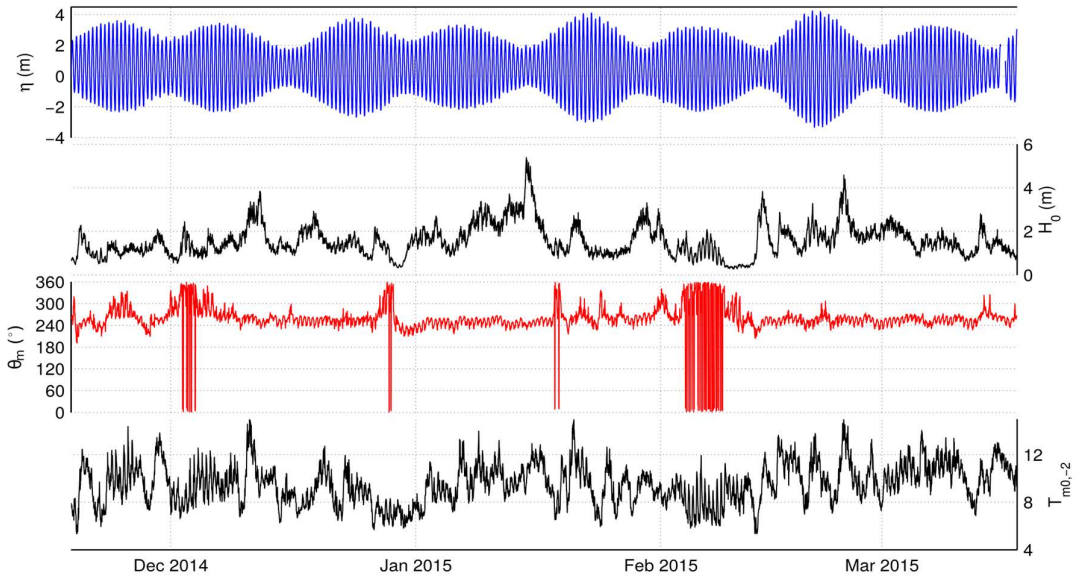

Figure 4. Time-series of offshore significant water level (first panel), significant wave height (second panel), mean wave direction (third panel), and mean wave period $T_{m0,-2}$ (last panel) from November 18 2014 to March 18 2015.

4.2. Wave runup during winter 2014/15

The pressure time-series recorded by the four pressure sensors installed on Banneg's cliffs were used to detect η_2 events between January 2014 and April 2015. A total of 345 events were detected during this period. No trends showed up in the number of events detected between the bottom and top sensors (Table 1), indicating that local detection of runup events was independent of the tidal stage. The distribution of runup events against offshore water levels (Fig.5), clearly shows the tidal stages that promoted runup detection at the four sensor locations. Although fewer events were detected at high-tide, the full tidal range was encompassed by our measurements. Regarding the offshore significant wave height associated to η_2, most runup events occurred with H_0 lower than 2.5 m. Also, P_1 did not detected any events associated to H_0 larger than 2.5 m and P_4 did not detected any events associated to H_0 lower than 1 m. This difference was attributed to the positions of the sensors with respect to the still water level. Indeed, the position of P_1 was systematically lower than the 2% shoreline elevation during energetic conditions, even at low tide.

Table 1. Number of runup events detected for each sensors and associated mean offshore significant wave height, mean water level, and mean, minimum and maximum η_2 .

	# events	Mean water level (m)	Mean H_s (m)	Mean η_2 (m)	$\eta_{2,\,min}$ (m)	$\eta_{2,\,max}$ (m)
P1	66	-1.6	1.3	0.5	0.0	1.5
P2	139	0.2	1.9	1.0	0.2	2.3
P3	112	1.5	1.7	1.2	0.2	3.6
P4	28	3.2	2.6	2.7	1.8	3.7

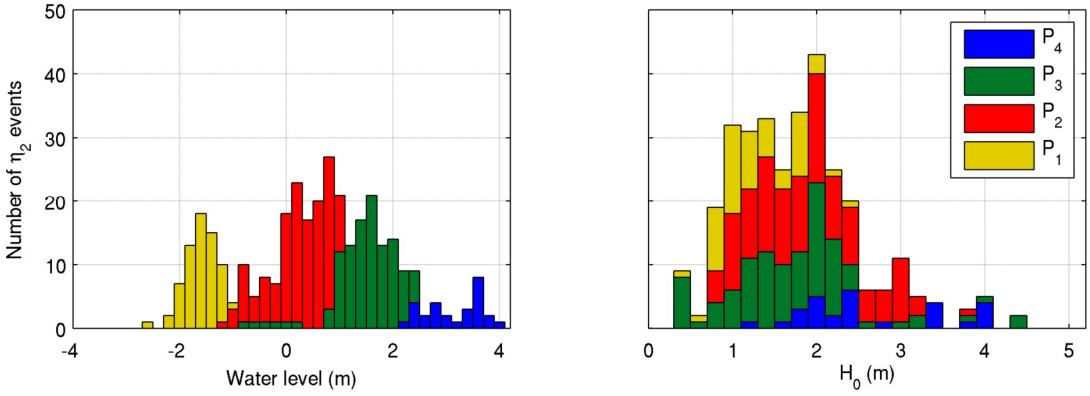

Figure 5. Histograms showing the number of η_2 events detected by each sensor against the offshore water level (left) and significant wave height (right).

On the contrary, P_4 was systematically dry during calm conditions, even at high tide. All in all, the largest number of detected events occurred with H_0 = 2.0 m. The time-series of η_2 detected by each sensor are shown on Fig. 6. On average, the bottom sensors measured lower runup than the top sensors (Table 1). Sensor P_4 measured the highest η_2 (3.7 m) on February 24 2015.

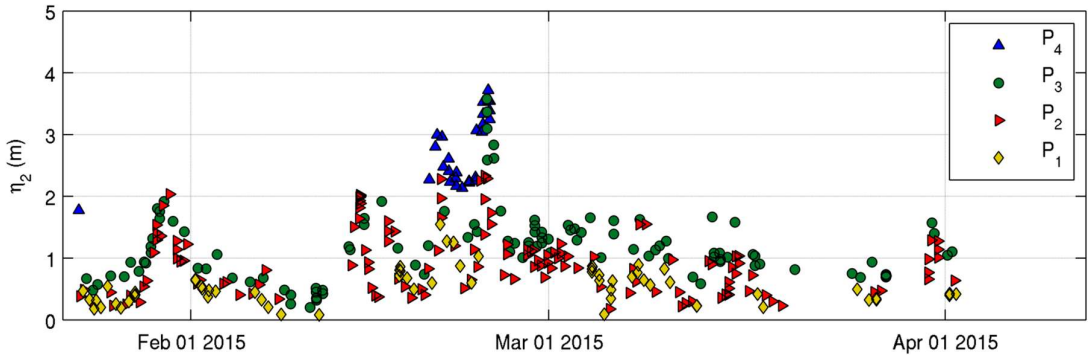

Figure 6. Time-series of η_2 from January 2014 to April 2015.

4.2.1. Wave runup dependence on offshore wave parameters

The wave runup is known to depend on the wave conditions and the beach morphology (Hunt, 1959; Holman, 1986; Stockdon *et al*., 2006). The relations between runup and offshore wave parameters were assessed through scatter diagrams of η_2 versus offshore significant wave height H_0, wave period $T_{m0,-2}$ and $(H_0L_0)^{0.5}$ (Fig.7). The corresponding squared correlations coefficients (ρ^2), are summarized in Table 2. Although many authors presented their results in non-dimensional space, with the runup parameter normalized by the offshore significant wave height, we performed our analysis with dimensional parameters in order to reduce the errors associated to small wave cases, as explained by Stockdon *et al*. (2006). Indeed, the scatter diagrams in non-dimensional space showed much more spread, resulting in poorer correlations and significant differences in the least-square coefficients compared to the ones obtained with the better correlated dimensional parameters. Fig.7a represents η_2 values against H_0 for the four sensors. The squared correlation coefficients ranged between 0.74 (P_1) and 0.85 (P_4), with an average of 0.79, indicating a good fit between η_2 and H_0. For the wave period, five spectral parameters were tested : the peak period T_p and the four integrated parameters $T_{m0,1}$, $T_{m0,2}$, $T_{m0,-1}$ and $T_{m0,-2}$. For these parameters, ρ^2 ranged between 0.15 and 0.65 (with p-values < 0.005), indicating a significant relationship between wave runup and wave period. Although the highest scores depended on which sensor was considered, the sensor-averaged scores revealed that T_p was the parameter that worst correlated with runup, and $T_{m0,-2}$ was

the one that best correlated with runup. The correlations between η_2 and $(H_0L_0)^{0.5}$ (where L_0 was inferred from $T_{m0,-2}$ using the linear theory) were very high (ρ^2 = 0.81) and confirmed the linear relationship existing between these parameters, already evidenced by various authors (e.g. Hunt, 1959; Holman, 1986; Stockdon *et al*., 2006; Suanez *et al*., 2015).

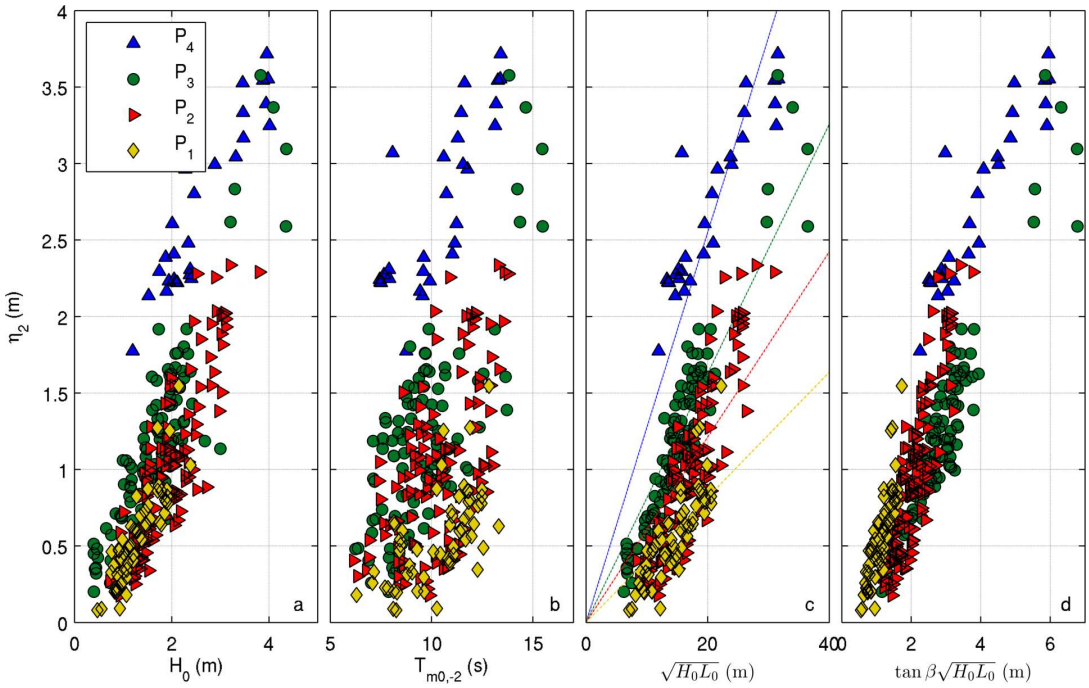

Figure 7. Scatter diagrams of η_2 versus H_0 (a), $T_{m0,-2}$ (b), $H_0L_0^{0.5}$ (c), and tanβ $H_0L_0^{0.5}$ (d)

Our data set clearly confirmed the existence of a quasi-linear relationship between η_2 and $(H_0L_0)^{0.5}$ for each individual sensor. However, significant differences appeared in the slopes and intercepts of the linear regression function (Fig.7c) fitted through the data set η_2 against $(H_0L_0)^{0.5}$ of each sensor. Indeed, these slopes were 0.04, 0.06, 0.08, and 0.13 for sensors P_1, P_2, P_3, and P_4, respectively. These differences likely traduced the impact of the foreshore slope on the wave runup.

Table 2. Squared correlation coefficients (ρ^2) between η_2 and offshore wave parameters.

	H_0	T_p	$T_{m0,1}$	$T_{m0,2}$	$T_{m0,-1}$	$T_{m0,-2}$	$H_0L_0^{0.5}$
P_1	0.74	0.32	0.44	0.44	0.43	0.41	0.73
P_2	0.77	0.23	0.29	0.29	0.30	0.31	0.78
P_3	0.79	0.15	0.50	0.48	0.53	0.53	0.89
P_4	0.85	0.46	0.61	0.64	0.62	0.65	0.86
MEAN	0.79	0.29	0.46	0.46	0.47	0.48	0.81

4.2.2. Wave runup dependence on the foreshore slopes

The impact of the foreshore slopes on the wave runup was investigated through the correlations between η_2 and $\tan\beta(H_0L_0)^{0.5}$. For each runup event detected by the pressure sensors, the slope was computed with the five methods defined in section 3, and the corresponding time-series of $\tan\beta(H_0L_0)^{0.5}$ were generated. The slopes computed with method M_1 were constant in time and identical for all sensors of each profile, to

provide a baseline method against which the four other methods were compared. This slope was equal to 0.18 and the squared correlation coefficient was 0.61. The slopes computed with method M_2 were constant in time and only depended on the sensors' location. These slopes were equal to 0.08, 0.12, 0.18, and 0.19, from P_1 to P_4, respectively. This method improved the correlations with a squared correlation coefficient $\rho^2 = 0.79$, i.e. 29% larger than the one obtained with the baseline method M_1. The mean slopes computed with method M_3 were comprised between 0.18 (P_1) and 0.22 (P_4), and the slope ranges (r) did not exceed 0.04. This method improved the correlations with a squared correlation coefficient $\rho^2 = 0.73$, i.e. 20% larger than the one obtained with M_1. The mean slopes computed with method M_4 were comprised between 0.15 (P_3) and 0.19 (P_4), and the slopes ranges were larger ($0.05<r<0.14$) with this method than with M_3. The squared correlation coefficient associated to this method was 0.37, 40% lower than the one obtained with M_1. Finally, the mean slopes computed with method M_5 were comprised between 0.12 (P_3) and 0.24 (P_2), and the slope ranges were the largest of all methods ($0.11<r<0.26$). The associated squared correlation coefficient was 0.30, i.e. 51% lower than the one obtained with M_1. These results clearly showed that the method used to compute the slopes was critical when assessing the correlations between η_2 and $\tan\beta(H_0L_0)^{0.5}$. While methods M_2 and M_3 provided evidence that the extreme runup values could be related to the slopes of the profile, methods M_4 and M_5 tended to show the opposite. The low scores obtained with methods M_4 and M_5 were linked to the large range of slope values computed with these methods. Indeed, during calm conditions, when η_2 and H_0 were low, the slopes were computed over narrow regions, mostly influenced by small-scale topographic gradients, and could reach values very different than the large-scale slope. Using a fixed horizontal extent to compute the slope, as with M_2 and M_3, prevented from giving too much importance to small scale features, while accounting for the large scale changes in the profile. Fig.7d shows the scatter diagrams between η_2 and $\tan\beta(H_0L_0)^{0.5}$ obtained with M_2 .

5. Discussion and Conclusion

The overall good fit between η_2 and $\tan\beta(H_0L_0)^{0.5}$ ($\rho^2 = 0.89$) revealed a linear relationship between these parameters. However, a direct comparison with the widely-used equations for R_2 predictions, such as the ones of Holman and Sallenger (1985) and Stockdon *et al*. (2006), was precluded because of the difference between η_2, the 2% exceedance level of shoreline elevation, and R_2, the 2% exceedance level of runup maxima. Holman (1986) analyzed video-based runup measurements on a mild-sloping beach and computed the relationships between the Iribarren number and several statistical parameters for extreme wave runup, including η_2. They obtained the following linear relation for the non-dimensional η_2

$$\frac{\eta_2}{H_0} = 0.75\xi_0 + 0.18 \tag{4}$$

and related the positive intercept 0.18 to the wave setup. Fig.8 shows the normalized η_2 against the Iribarren number computed with our data set. The least-square regression slope obtained for the rocky cliffs of Banneg Island (0.30, blue line) is much lower than the one obtained by Holman (1986) for sandy beaches (0.75, black line), suggesting that additional processes may impact the runup propagation on rocky coasts compared to sandy beaches. Although this difference can be partly attributed to the complex topography of Banneg Island, (e.g. the presence of headlands), which necessarily impacts the wave propagation from the deep water to the cliff, it is reasonable to relate this difference to the nature of the bottom in both study sites. Indeed the frictional forces acting on the swash bore propagation should be larger on rocky bottom, and therefore attenuate the wave runup. For instance, Meer and Stam (1992) investigated the propagation of wave runup over coastal structures and observed that wave runup was much lower (up to 50%) over rocky slopes than over smooth slopes. These considerations raise the need to further investigate wave runup physics on a large panel of environments, in order to better understand the impact of frictional forces on swash propagation, and improve the accuracy of extreme runup predictions.

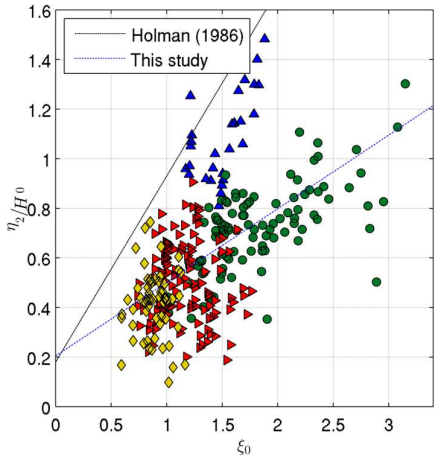

Figure 8. Scatter diagrams of η_2/H_0 versus ξ_0.

Acknowledgements

We warmly thank the Réserve naturelle d'Iroise and its rangers H. Maheo and D. Bourles for allowing us to perform the measurements and helping in many ways our access to the site. Many thanks also go to the technical group at the French Navy Hydrographic and Oceanographic Institute (SHOM) who deployed and recovered the instruments. The Litto3D coastal digital elevation model co-produced by IGN and SHOM from numerous Lidar and MBES surveys was of great help in this project. This work is part of the research program PROTEVS (research contract 12CR6) funded by DGA and conducted by SHOM. This research was also supported by the "Laboratoire d'Excellence" LabexMER (ANR-10-LABX-19) and co-funded by the French government under the program "Investissements d'Avenir", and the region of Brittany. The atmospheric pressure data, the wave observations at Les Pierres Noires buoy, and the model outputs of the wave hindcast, were kindly provided by Meteo-France, CEREMA and IFREMER institutes.

References

Ardhuin, F., Roland, A., Dumas, F., Bennis, A.-C., Sentchev, A., Forget, P., Wolf, J., Girard, F., Osuna, P., and Benoit, M., 2012. Numerical Wave Modeling in Conditions with Strong Currents : Dissipation, Refraction, and Relative Wind. *Journal of Physical Oceanography*, 42(12):2101–2120.

Autret, R., Dodet, G., Fichaut, B., Suanez, S., David, L., Leckler, F., Ardhuin, F., Ammann, J., Grandjean, P., Allemand, P., and Filipot, J.-F., 2016. A comprehensive hydro-geomorphic study of cliff-top storm deposits on Banneg Island during winter 2013–2014. *Marine Geology,* 382:37-55.

Battjes, J. A., 1974. Surf similarity. *Coastal Engineering Proceedings*, 1(14).

Blenkinsopp, C. E., Matias, A., Howe, D., Castelle, B., Marieu, V., and Turner, I. L., 2016. Wave runup and overwash on a prototype-scale sand barrier. *Coastal Engineering*, 113:88–103.

Boudière, E., Maisondieu, C., Ardhuin, F., Accensi, M., Pineau-Guillou, L., and Lepesqueur, J., 2013. A suitable metocean hindcast database for the design of Marine energy converters. *International Journal of Marine Energy*, 3–4:40–52.

Bowen, A. J., Inman, D. L., and Simmons, V. P., 1968. Wave 'set-down' and set-Up. *Journal of Geophysical Research*, 73(8):2569–2577.

Camenen, B. and Larson, M., 2007. Predictive Formulas for Breaker Depth Index and Breaker Type. *Journal of Coastal Research*, 1028–1041.

Fichaut, B. and Hallégouët, B., 1989. Banneg, une île dans la tempête. *Penn ar Bed*, 135 :36–43.

Fichaut, B. and Suanez, S., 2011. Quarrying, transport and deposition of cliff-top storm deposits during extreme events : Banneg Island, Brittany. *Marine Geology*, 283(1–4):36–55.

Guedes, R. M. C., Bryan, K. R., and Coco, G., 2013. Observations of wave energy fluxes and swash motions on a low-sloping, dissipative beach. *Journal of Geophysical Research : Oceans*, 118(7) :3651–3669.

Guza, R. T. and Thornton, E. B., 1982. Swash oscillations on a natural beach. *Journal of Geophysical Research : Oceans*, 87(C1) :483–491.

Holland, K. T. and Holman, R. A., 1993. The statistical distribution of swash maxima on natural beaches. *Journal of Geophysical Research : Oceans*, 98(C6) :10271–10278.

Holland, K. T., Holman, R. A., Lippmann, T. C., Stanley, J., and Plant, N., 1997. Practical use of video imagery in nearshore oceanographic field studies. *IEEE Journal of Oceanic Engineering*, 22(1):81–92.

Holland, K. T., Raubenheimer, B., Guza, R. T., and Holman, R. A., 1995. Runup kinematics on a natural beach. *Journal of Geophysical Research : Oceans*, 100(C3) :4985–4993.

Holman, R. A., 1986. Extreme value statistics for wave run-up on a natural beach. *Coastal Engineering*, 9(6):527–544.

Holman, R. A. and Guza, R. T., 1984. Measuring run-up on a natural beach. *Coastal Engineering*, 8(2) :129–140.

Holman, R. A. and Sallenger, A. H., 1985. Setup and swash on a natural beach. *Journal of Geophysical Research : Oceans*, 90(C1):945–953.

Hunt, I., 1959. Design of Seawalls and Breakwaters. *Journal of the Waterways and Harbors Division*, 85(3) :123–152.

Huntley, D. A., Guza, R. T., and Bowen, A. J., 1977. A universal form for shoreline run-up spectra? *Journal of Geophysical Research*, 82(18) :2577–2581.

Iribarren, C. and Nogales, C., 1949. Protection des Ports. *In XVIIth International Navigation Congress*, Section II, Communication 4, 31–80, Lisbon, Portugal.

Kobayashi, N., Cox, D. T., and Wurjanto, A., 1991. Permeability Effects on Irregular Wave Runup and Reflection. *Journal of Coastal Research*, 7(1):127–136.

Louvart, L. and Grateau, C., 2005. The Litto3d project. In *Europe Oceans 2005*, volume 2, pages 1244–1251 Vol. 2.

Masselink, G. and Puleo, J. A., 2006. Swash-zone morphodynamics. *Continental Shelf Research*, 26(5):661–680.

Masselink, G., Scott, T., Poate, T., Russell, P., Davidson, M., and Conley, D., 2015. The extreme 2013/14 winter storms : hydrodynamic forcing and coastal response along the southwest coast of England. *Earth Surface Processes and Landforms*, 41:378-391.

Meer, J. W. v. d. and Stam, C.-J. M., 1992. Wave Runup on Smooth and Rock Slopes of Coastal Structures. *Journal of Waterway, Port, Coastal, and Ocean Engineering*, 118(5):534–550.

Phillips, O. M., 1984. On the Response of Short Ocean Wave Components at a Fixed Wavenumber to Ocean Current Variations. *Journal of Physical Oceanography*, 14:1425–1433.

Poate, T. G., McCall, R. T., and Masselink, G., 2016. A new parameterisation for runup on gravel beaches. *Coastal Engineering*, 117:176–190.

Raubenheimer, B. and Guza, R. T., 1996. Observations and predictions of run-up. *Journal of Geophysical Research : Oceans*, 101(C11):25575–25587.

Roland, A. and Ardhuin, F., 2014. On the developments of spectral wave models : numerics and parameterizations for the coastal ocean. *Ocean Dynamics*, 64(6):833–846.

Ruessink, B. G., Kleinhans, M. G., and van den Beukel, P. G. L., 1998. Observations of swash under highly dissipative conditions. *Journal of Geophysical Research : Oceans*, 103(C2):3111–3118.

Ruessink, B. G., Walstra, D. J. R., and Southgate, H. N., 2003. Calibration and verification of a parametric wave model on barred beaches. *Coastal Engineering*, 48(3):139–149.

Ruggiero, P., Holman, R., and Beach, R., 2004. Wave run-up on a high-energy dissipative beach. *Journal of Geophysical Research C : Oceans*, 109(6).

Ruggiero, P., Komar, P. D., McDougal, W. G., Marra, J. J., and Beach, R. A., 2013. Wave Runup, Extreme Water Levels and the Erosion of Properties Backing Beaches. *Journal of Coastal Research*, 17(2).

Sallenger, A. H., 2012. Storm Impact Scale for Barrier Islands. *Journal of Coastal Research*, 16(3).

Salmon, J. E., Holthuijsen, L. H., Zijlema, M., van Vledder, G. P., and Pietrzak, J. D., 2015. Scaling depth-induced wave-breaking in two-dimensional spectral wave models. *Ocean Modelling*, 87:30–47.

Senechal, N., Coco, G., Bryan, K. R., and Holman, R. A., 2011. Wave runup during extreme storm conditions. *Journal of Geophysical Research:Oceans*, 116(C7) :C07032.

SHOM, 2014. *Références Altimétriques Maritimes. Côtes du zéro hydrographique et niveaux caractéristiques de la marée*. Service hydrographique et océanographique de la Marine, Brest.

SHOM, 2016. *Courant de marées : Mer d'Iroise, de l'Ile Vierge à la pointe de Penmarc'h*, volume 56.

Stockdon, H. F., Holman, R. A., Howd, P. A., and Sallenger Jr., A. H., 2006. Empirical parameterization of setup, swash, and runup. *Coastal Engineering*, 53(7):573–588.

Suanez, S., Cancouët, R., Floc'h, F., Blaise, E., Ardhuin, F., Filipot, J.-F., Cariolet, J.-M., and Delacourt, C., 2015. Observations and Predictions of Wave Runup, Extreme Water Levels, and Medium-Term Dune Erosion during Storm Conditions. *Journal of Marine Science and Engineering*, 3(3):674–698.

Suanez, S., Fichaut, B., and Magne, R., 2009. Cliff-top storm deposits on Banneg Island, Brittany, France : Effects of giant waves in the Eastern Atlantic Ocean. *Sedimentary Geology*, 220(1-2) :12–28.

Vousdoukas, M. I., Wziatek, D., and Almeida, L. P., 2012. Coastal vulnerability assessment based on video wave run-up observations at a mesotidal, steep-sloped beach. *Ocean Dynamics*, 62(1) :123–137.